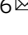## ARTICLE

Check for updates

Runup of landslide-generated tsunamis controlled by paleogeography and sea-level change

Qiliang Sun [1,2✉], Qing Wang[1], Fengyan Shi[3], Tiago Alves [4], Shu Gao [5], Xinong Xie[1], Shiguo Wu[6✉] & Jiabiao Li[7]

Pre-Holocene landslides and tsunami deposits are commonly observed on continental margins and oceanic islands. However, scarce evidence has thus far linked pre-historic submarine landslides to particular tsunami events. This work focuses on an 839 km^3 submarine landslide that occurred in the South China Sea at 0.54 Ma. Bathymetric restorations show that the paleoshoreline at 0.54 Ma was 180–580 km to the south of its present-day location. In such a setting, the tsunami triggered by the landslide at 0.54 Ma was able to generate larger waves with shorter arrive times when compared to an equivalent landslide-generated tsunami under present-day conditions. This observation proves that tsunamis generated by submarine landslides during sea-level lowstands caused catastrophic damage to the South China Sea coast in the past, and so will do in future sea-level lowstands. This study stresses the importance of restoring paleoshorelines for detailed analysis of historic landslide-generated tsunamis.

[1] Hubei Key Laboratory of Marine Geological Resources, China University of Geosciences, 430074 Wuhan, China. [2] Laboratory for Marine Mineral Resources, Qingdao National Laboratory for Marine Science and Technology, 266061 Qingdao, China. [3] Center for Applied Coastal Research, University of Delaware, Newark, DE 19716, USA. [4] 3D Seismic Laboratory, School of Earth and Environmental Sciences, Cardiff University, Main Building, Park Place, Cardiff CF10 3AT, UK. [5] Department of Coastal Ocean Science, School of Geographic and Oceanographic Sciences, Nanjing University, 210023 Nanjing, China. [6] Laboratory of Marine Geophysics and Georesources, Institute of Deep-sea Science and Engineering, Chinese Academy of Sciences, 572000 Sanya, China. [7] Key Laboratory of Submarine Geosciences, Second Institute of Oceanography, Ministry of Natural Resources, 310012 Hangzhou, China. ✉email: sunqiliang@cug.edu.cn; swu@idsse.ac.cn

Tsunamis generated by submarine landslides may be catastrophic to life and infrastructure along low-lying shores of ocean islands and continental margins[1–8]. Their detailed analysis has become particularly important after the 1998 tsunami of Papua New Guinea, during which some 2200 people lost their lives because vast swathes of the Papuan coast were hit by giant waves[9,10]. However, in comparison to earthquake-generated tsunamis, those generated by submarine landslides are still poorly understood due to the limited availability of historical data on such events[11]. While a few well-preserved paleotsunami deposits are documented in the literature, such as those on the Central Atlantic[12,13] and Shetland Islands[14], most paleotsunamis generated by submarine landslides are either poorly preserved in the geological record, being identified a long time after they occur, or are usually identified only via the interpretation of high-resolution bathymetric data from the regions affected by such phenomena[14–18]. Resultant deposits are often poorly preserved on affected coastal areas, tend to be overprinted by human activity, or lack diagnostic features—unlike those associated with earthquake-induced tsunamis[19]. As a result of these limitations, mathematical models became the main approach followed by the scientific community to study past tsunamis induced by submarine landslides[15,17,20–26]. Relatively young landslides such as those recorded in the Messina Strait in 1908[27], off Papua New Guinea coast in 1998[9,10,28], in the Sunda Strait in 2018[4,29], and in Palu in 2018[30–32], were successfully simulated to identify their physical parameters, and corroborate mathematical models and field-derived information.

Mathematical models that use readily emplaced landslide parameters (i.e., length, width, thickness) and present-day digital elevation data for landslide-generated tsunamis[5,9,15,27,32–34] are valid for relatively young tsunamis because sea-level variations, temporal and spatial changes in sediment accumulation rates, and resultant paleogeographic changes, are negligible for such a short time interval, as in the case of the Tohoku and Kanto regions of Japan[35] and the Alas Strait of Indonesia[36]. For older landslides (e.g., the ~8200 b.p. Storegga Slide[14,15]), mathematical models may still be helpful, but the relative position of the paleoshoreline and nearby paleobathymetric features may not match the present-day's coastal and submarine topographies. To better understand tsunamis generated by ancient submarine landslides, it is crucial to reconstruct the paleobathymetry, paleoshoreline position, and constrain the exact dimensions of relatively old submarine landslides. Realistic scenarios for pre-historic tsunamis cannot be obtained by the mere use of present-day digital elevation data.

Here, we use high-quality geophysical data, borehole information, and numerical models to investigate the 0.54 Ma old Baiyun Slide of the South China Sea (Fig. 1). The aim is to restore the regional paleoshorelines, and explore the impact of modeled paleotsunamis on these latter. Ultimately, this study shows how changes in coastline position and regional bathymetry greatly affect tsunami-wave propagation and, subsequently, its impact on coastal regions.

Environmental setting of the study area. The South China Sea is the largest (>3,500,000 km²) marginal sea in the western Pacific Ocean and is bounded to the east by the Manila Trench (Fig. 1). Its northern continental margin has recorded high sedimentation rates in the order of 12.2–19.3 cm/ky since the middle Miocene[37–39]. Fine-grained hemipelagic sediment, mainly derived from the Pearl River and Red River drainage systems (Fig. 1), have predominated in deep-water areas of the northern South China Sea since the early Pliocene[40].

Coastal areas surrounding the South China Sea are particularly vulnerable to large tsunami waves due to their ever-growing population and infrastructure, most of which occupy low-lying areas[8]. At the broader regional scale, mega-earthquakes in the Manila Trench are recognized as the main source of tsunamis in the South China Sea[8,41,42]. Slope instability is also common in this region, as documented by the Baiyun and Brunei Slides[39,43–50], implying that submarine landslides can also generate tsunamis. In some areas of the northern South China Sea, the continental slope is highly unstable, and multiple Quaternary mass-transport deposits (MTDs) were previously identified in geophysical data[39,44–51]. Among these MTDs, the Baiyun Slide covers an area of 11,000 km² for a conservative volume of 1035 km³ in the northern South China Sea[39,48]. It unraveled as a minimum of four failure events referred to in the literature, from top to bottom, as MTDa (0.18 Ma), MTDb (0.54 Ma), MTDc (0.79 Ma), and MTDd (1.59 Ma), based on the interpretation of seismic reflection data and synthetic seismograms tying known biostratigraphic ages to seismic reflectors[39,49]. The largest of these four mass-transport deposits, MTDb, with a volume of 839 km³, is the focus of this study (Fig. 1). The presence of interbedded coarse- and fine-grained sediments on the continental slope, variations in relative sea level, progradational and retrogradational phases in the Pearl River Delta, pockets of free gas below the seafloor, and localized weakening of sediment by faults, are the main factors preconditioning slope instability near the Baiyun Slide[39].

Results

Geophysical character of submarine landslides. MTDb occurred at 0.54 Ma[39] and resulted in the worst-case tsunami scenario, as it records the largest volume when compared to other MTDs in the region. MTDb is 252 km long from the headscarp to its fan-like distal part (Fig. 2). It is identified at a water depth between 940 m and 3090 m, on a continental slope averaging 0.65° in gradient at present (Fig. 2a). Evidence for the occurrence of past slope instability near MTDb includes the presence of a large and curved 14–47 km-wide seafloor escarpment (Figs. 2 and 3). The gradient of this escarpment is >5°, locally reaching 15°. Its height ranges from 10 m to 185 m. On selected seismic profiles, failed strata are shown as chaotic to transparent intervals often accompanied by remnant (in-situ) and rafted (floating) blocks (Fig. 3). Thrust faults that are typical of the toe areas of MTDs are not present in the distal part of MTDb (Fig. 3d). Failed strata were totally evacuated from MTDb's eastern part, whilst its western part was locally evacuated (Figs. 2b and 3a–c). Hence, the failed sediment was transported toward the ocean basin[39].

Failed sediment flowed along the axis of a central depression as suggested by: (a) the present-day bathymetry (Fig. 2a), (b) the presence of linear grooves on the basal surface of MTDb[39], and (c) the residual thickness of failed strata associated with MTDb (Fig. 2b). Thus, MTDb covers an area of 5500 km² on the continental slope, with a residual depositional zone of 3166 km² and an evacuation zone of 2334 km². Its residual volume, i.e., the volume of failed sediment on the continental slope, is 222 km³ (Fig. 2b).

The distal part of MTDb in the ocean basin represents a depositional zone that covers an area of 5603 km², for a conservative volume estimate of 617 km³ (see ref. [48]). Here, mass-transport deposits form a fan-like depositional body with a diameter of 42 km in the ocean basin. These same deposits flowed across a 9–14 km wide pass, or bight, located at the continent-ocean boundary (Fig. 2b). Similar to failed strata on the continental slope, this sediment fan comprises chaotic to transparent seismic reflections lacking internal structures (Fig. 3d). MTDb is therefore interpreted as a debris flow,
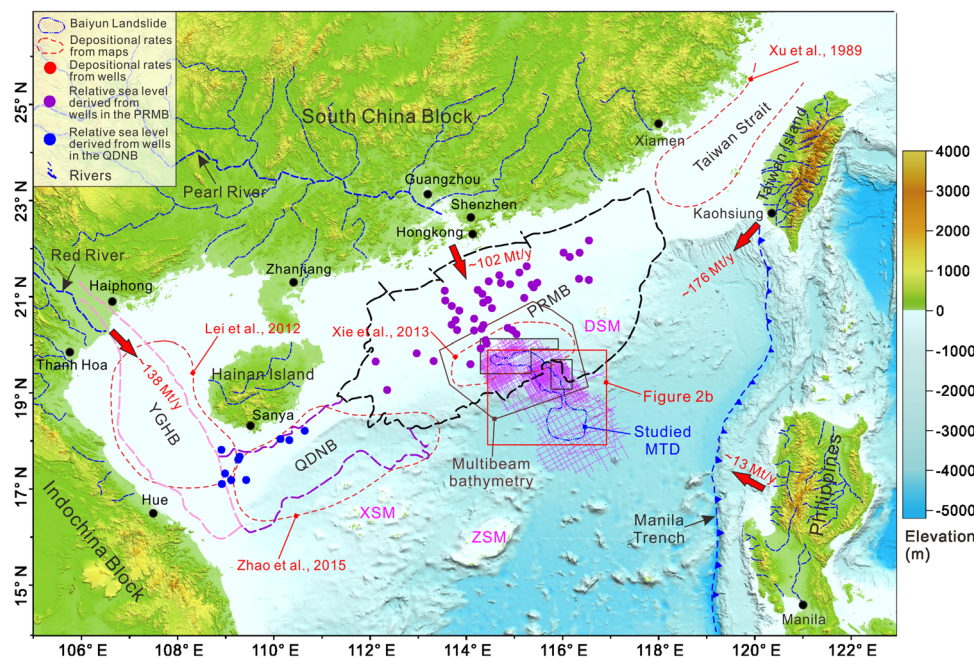
Fig. 1 Geological setting of the study area. Major basins such as the Pearl River Mouth Basin (PRMB, shown with a black dashed line), Qiongdongnan Basin (QDNB, shown with a purple dashed line), Yinggehai Basin (YGHB, shown with a light pink dashed line) are marked in the figure. The studied submarine landslide is delimited by a blue dashed line. Pink dashed lines and black squares highlight the 2D and 3D seismic data used in this study. The brown solid polygon refers to the multibeam bathymetric data. Sedimentation rates calculated from thickness maps in refs. [38,58,67,68] are shown by red dashed lines. Other well locations used to calculate sedimentation rates are shown in Supplementary Table S1. Exploration wells are used to restore relative sea-level changes in the Pearl River Mouth Basin (see purple circles)[55], and in the Qiongdongnan and Yinggehai basins (see blue circles)[53]. Values of river discharge (see red arrows with black boundaries) are based on ref. [76]. Manila Trench is modified from ref. [45]. DSM Dongsha Massif, XSM Xisha Massif, ZSM Zhongsha Massif.

according to the similar seismic character of debrites documented worldwide[16,52]. The present-day water depth of the ocean basin where MTDb is located ranges from 3600 to 3800 m, with an average gradient of 0.13° on top of the fan (Fig. 2a). Considering that the total volume of failed sediment is 839 km^3 (i.e., 222 km^3 on the continental slope and 617 km^3 in its distal, ocean basin), and covers an area of 5500 km^2, we estimate a conservative thickness of 153 m for this deposit.

Restoration of paleoshorelines. Relative sea level is, at present, 20.2 m higher in the Qiongdongnan Basin[53,54], and 160.1 m higher in the Pearl River Mouth Basin[55] when compared to its position at 0.54 Ma. Hence, considering relative sea-level change alone, the paleoshorelines of the northern South China Sea at 0.54 Ma were located 110 km to 240 km oceanward (i.e., southward) from their present-day positions, and the entire continental shelf (including the Taiwan Strait) was sub-aerially exposed at that time. Thus, relative sea level had a profound influence on the paleobathymetry of the continental shelf of the northern South China Sea (Supplementary Fig. S1a). Comparatively, the continental shelf bordering Vietnam and the northwestern part of South China Sea around the Yinggehai Basin were not affected by sea-level change to the same degree. In these regions, the shoreline shifted 1 km to 33 km oceanward at 0.54 Ma (Supplementary Fig. S1b).

When only considering the effect of sediment supply on shoreline position, the Yinggehai Basin at 0.54 Ma became almost entirely sub-aerial due to the large volume of sediment derived from the Red River (Supplementary Fig. S1b), which fed sediment to the shelf at a rate of 21 × 10^3 km^3/Ma to 86.9 × 10^3 km^3/Ma since 5.5 Ma[56–58]. Except for the Taiwan Strait and its surrounding areas, high sediment supply (Supplementary Table S1) would

have caused the paleoshoreline of the northern South China Sea to advance oceanward by 90 to 150 km at 0.54 Ma (Supplementary Fig. S1). Hence, the Yinggehai Basin to the northwest was noticeably more sensitive to the effect of sediment supply on its paleowater depth (Supplementary Fig. S1).

We restored the paleobathymetry and shoreline positions of the northern South China Sea at 0.54 Ma taking into account both relative sea-level change and sediment supply (Fig. 4). The restoration shows that the northern paleoshoreline was located 180–580 km oceanward from its modern position, and nearly all the northern continental shelf was sub-aerially exposed at 0.54 Ma. The paleoshoreline was located near, or slightly to the north (10–20 km), of the present-day shelf break (Fig. 4). In the eastern South China Sea, where the continental shelf is narrow, the paleoshoreline shifted oceanward by only 10–30 km at 0.54 Ma (Fig. 4).

Model output for paleotsunamis. We modeled slope failure scenarios and their associated tsunamis according to the restored paleobathymetry at 0.54 Ma and geological constraints (including area, thickness, and volume of MTDb) gathered from geophysical data (Figs. 5–8). A simulation considering the present-day bathymetry was also carried out for comparison. In the present-day model, the failed strata gradually move downslope following a preferential NW-SE direction, thus agreeing with the interpreted geophysical data (Figs. 2b and 5). Strata in the northern edge of the model are almost completely evacuated, with a resulting area of sediment accumulation to the south (Fig. 5a–c). This character also justifies the depositional patterns identified in seismic data (Fig. 2b). In the present-day model, tsunami waves radiate from the region of slope failure and propagate predominately to the SE in a
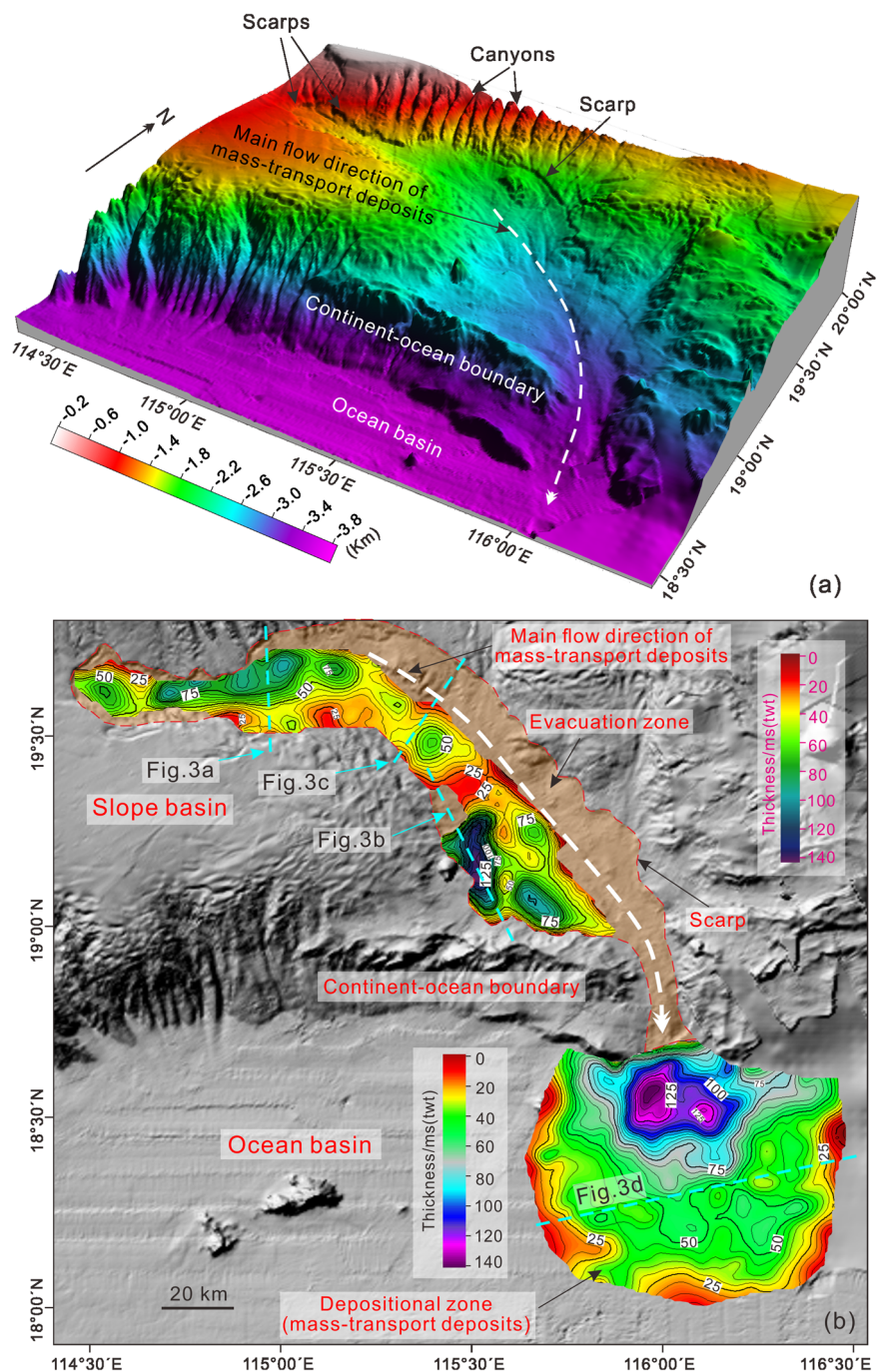
Fig. 2 3D visualization of the present-day seafloor and total thickness of mass-transport deposits. a 3D visualization of the present-day seafloor of the Pearl River Mouth Basin. Identified in the figure are the head and side scarps of the studied Baiyun Slide plus the continent-ocean boundary separating the slope area from the ocean basin. The main flow direction of failed sediment in the Baiyun Slide is shown by the white dashed line with an arrow; **b** total thickness of mass-transport deposits imaged by seismic reflection data in the study area. The sediments on the continental slope in the eastern part of Baiyun Slide were totally evacuated and deposited as a sediment fan in the ocean basin of South China Sea (marked as the depositional zone in the figure).

direction parallel to the movement of failed sediment. Conversely, they propagate slowly on the shallow, wide shelf of the northern South China Sea (Fig. 6a–c). The first tsunami wave arrives at the nearest northern shoreline ~150 min after the onset of MTDb, but arrives earlier at the nearest eastern shoreline after ~48 min (Table 1). A maximum wave height of ~5 m occurs along both the northern and eastern shorelines (Table 1).

In the 0.54 Ma tsunami model, the failed sediment is transported and accumulated (Fig. 5d–f) following a similar sequence of events to the present-day scenario previously described (Fig. 5a–c). Therefore, tsunami waves also radiate and propagate predominantly to the SE (Fig. 6d–f). Maximum wave height on the northern and eastern shorelines reaches ~18 m and ~10 m (Table 1), respectively (Figs. 7 and 8). Half of the northern shoreline is flooded by a 4 m-high tsunami in the 0.54 Ma model, while most of the eastern shoreline is flooded by a 2 m-high tsunami. The tsunami waves arrive at the nearest, northern South China Sea region in only 8 min, compared to the 150 min estimated in the present-day model (Table 1). At the nearest
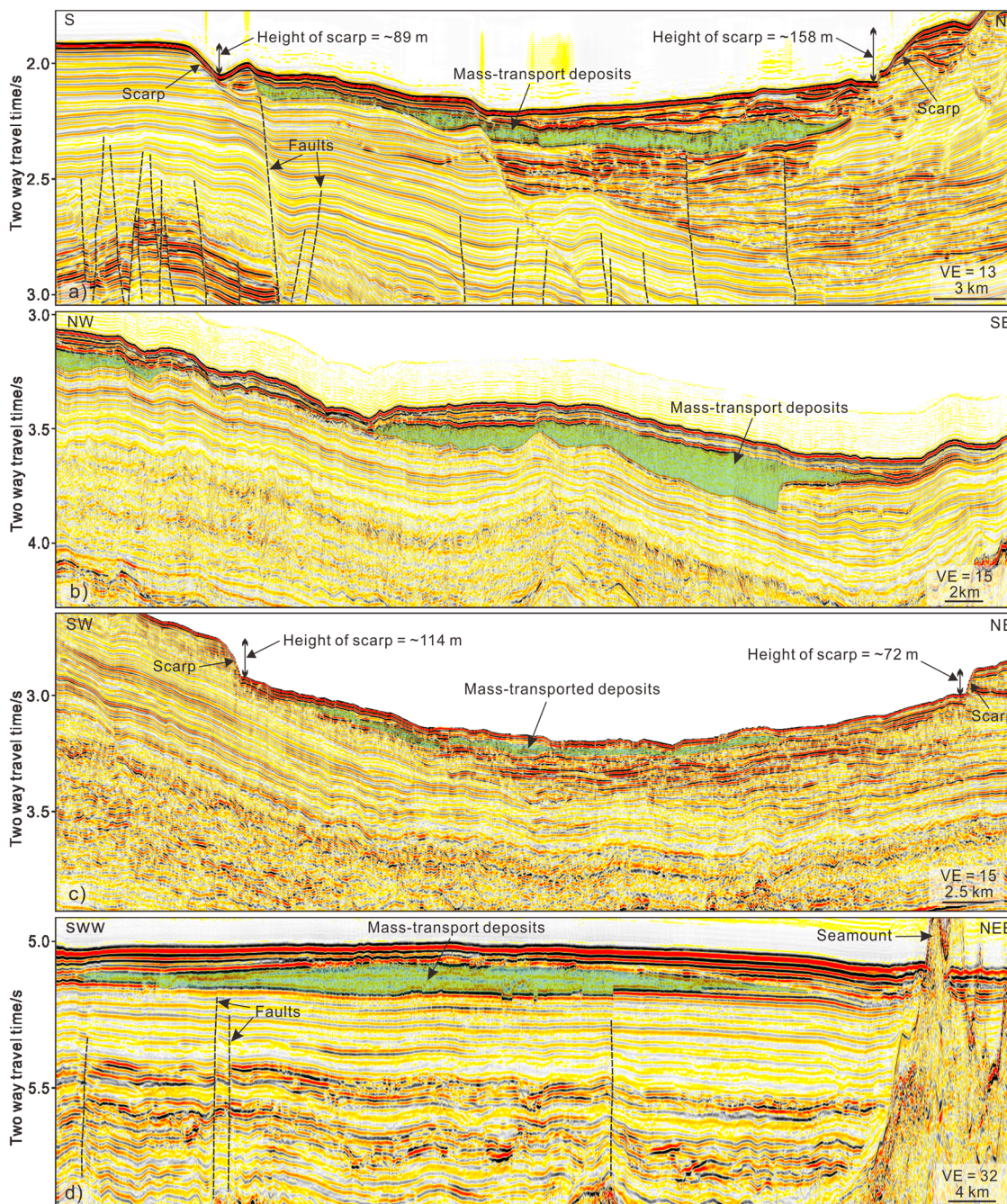
Fig. 3 Seismic character of mass-transport deposits. a–c Seismic character of mass-transport deposits on the continental slope. Failed strata show chaotic to transparent seismic reflections and internal deformation is not clearly imaged. Tall bounding scarps are also observed; **d** seismic character of failed strata in the ocean basin, which is similar to the character of failed strata in the slope basin. See the location of seismic profiles in Fig. 2b. VE vertical exaggeration.

eastern shoreline, tsunami waves arrive in 47 min, a value similar to the 48 min of the present-day model (Table 1).

The restored seabed morphology denotes wave propagation and evolution patterns that differ from the present-day scenario. Compared to the present-day, larger waves at 0.54 Ma occur near the shore due to lower dissipation of energy and more significant wave shoaling effect, which much enhances wave runups on the northern shoreline. In addition, the Dongsha Islands reflect and diffract the tsunami waves in the 0.54 Ma model, a character resulting in a distinct wave-height distribution behind the islands (Figs. 7a and 8a).

Discussion

The two sediment failure models considered in this study reveal similar characteristics, namely equivalent shapes, thickness and flow directions for failed strata, and agree with the observations gathered from seismic data (Figs. 2b and 5). While water depth has a limited influence on the movement and distribution of failed strata, our mathematic models show that bathymetry markedly controls tsunami-wave propagation and the impact of such waves on the coast (Figs. 6–8).

The large dataset used in this analysis, consisting of 53 exploration wells, bathymetric and seismic data, is accurate when
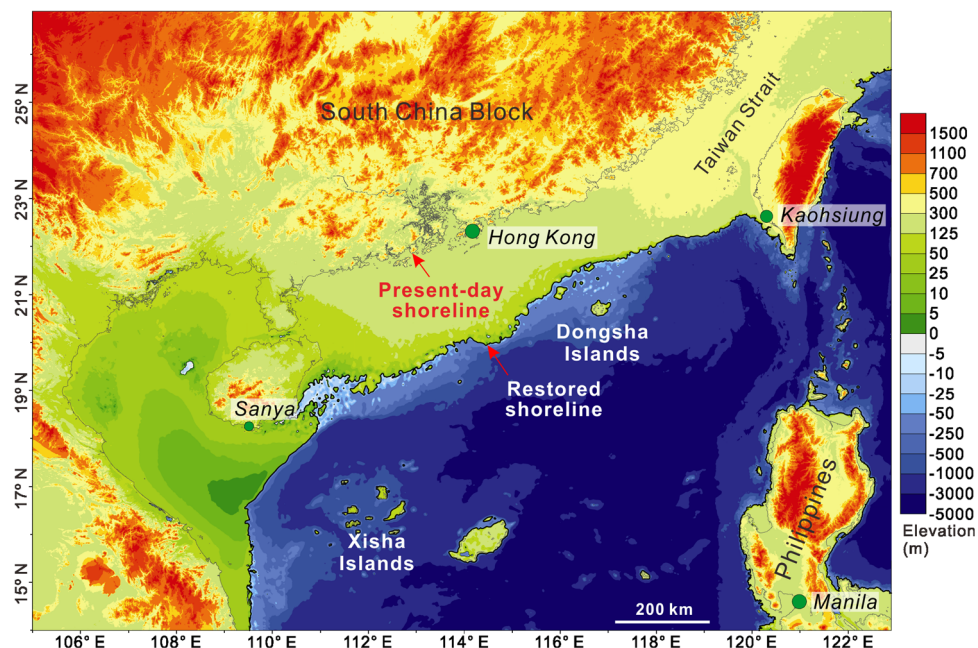
Fig. 4 Restoration of paleoshorelines and paleobathymetry at 0.54 Ma. The restoration shown considers both the relative sea-level change and sediment supply. The restored paleoshorelines are located several hundred kilometers oceanward, close to the present-day shelf break. See Supplementary Fig. S1 for the restoration of paleoshorelines at 0.54 Ma only considering the effect of relative sea-level changes and sediment supply.
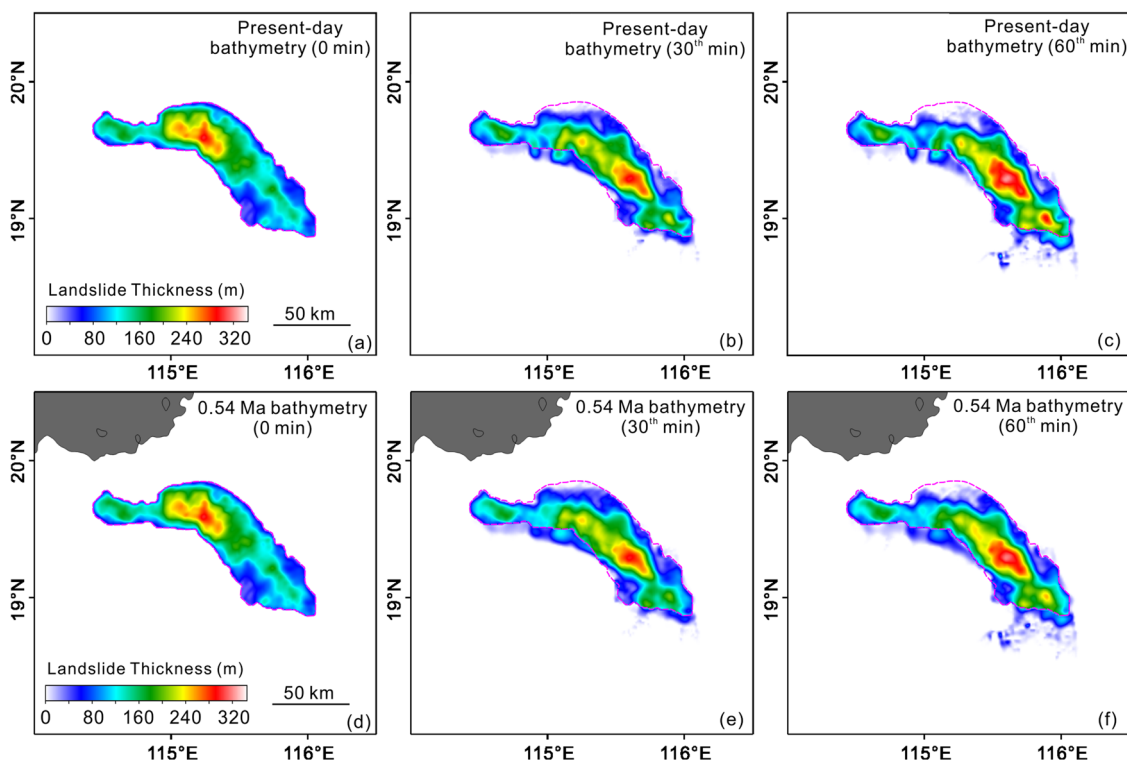

Fig. 5 Modeled movement of failed sediment. a–c Modeled movement of failed sediment and its distribution at 0, 30, and 60 min considering the present-day bathymetry and shoreline position. **d–f** Modeled movement of failed sediment and distribution at 0, 30, and 60 min considering the 0.54 Ma bathymetry and shoreline position. Bathymetry has a reduced influence on the movement of failed sediment and its distribution.

considering past sea-level curves and sediment supply to the margin, allowing a reliable restoration of the northern South China Sea's paleoshoreline. The 0.54 Ma paleobathymetry, occurred during a sea-level lowstand, implies in our models that the tsunami wave generated by MTDb at that time flooded the paleoshoreline region close to the modern shelf break (Fig. 4).

The tsunami wave height on the shoreline was also greatly enhanced in the 0.54 Ma model. For example, maximum wave height is much larger in the northern (~18 m) and eastern (~10 m) shorelines than the values calculated in present-day tsunami model, which estimates wave heights of ~5 m (Table 1). A reduced water depth in the source area of the tsunami, together
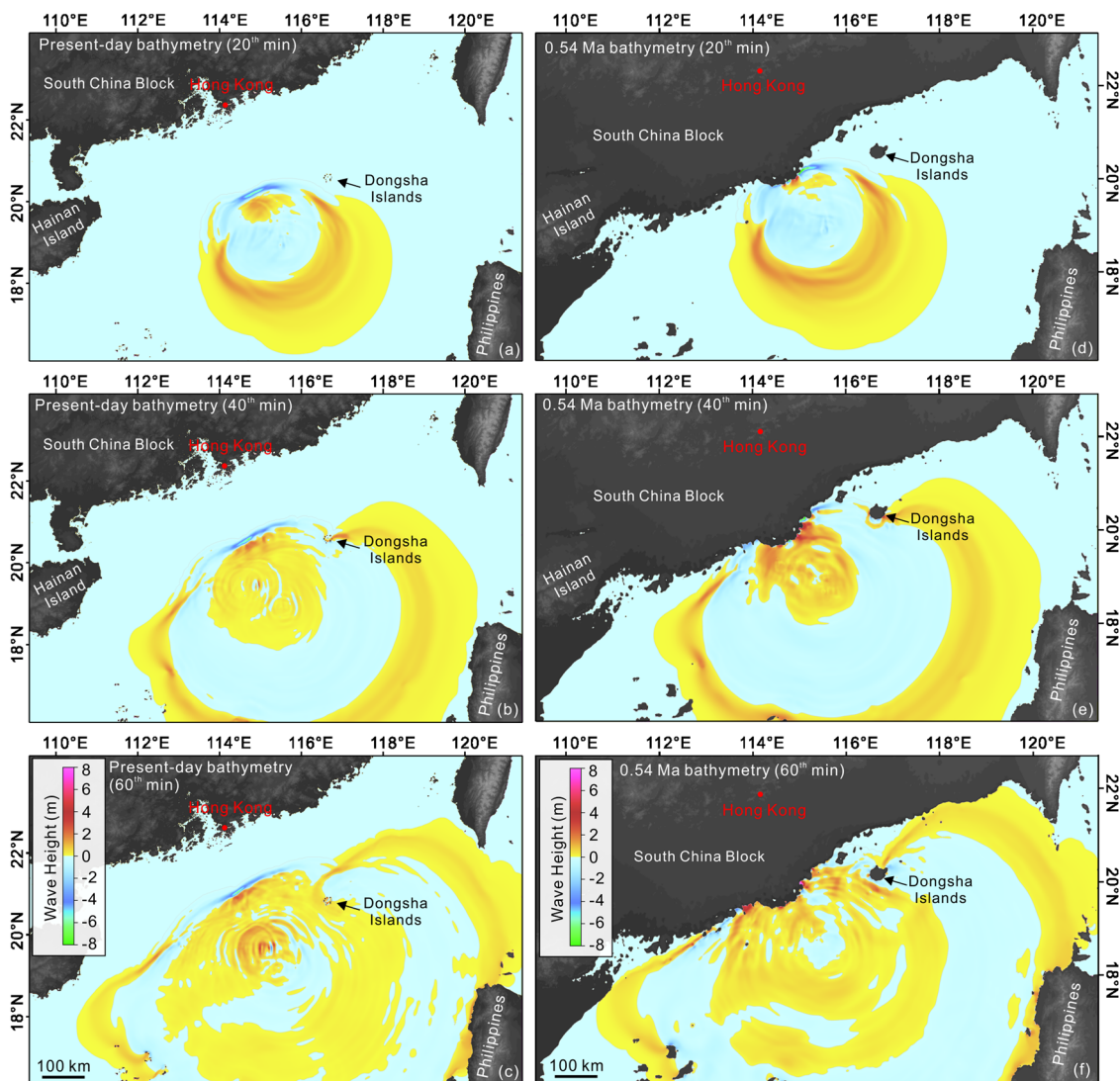
Fig. 6 Tsunami-wave propagation. a–c Tsunami-wave propagation at 20, 40, and 60 min bearing in mind the present-day bathymetry and shoreline position; **d–f** Tsunami-wave propagation at 20, 40, and 60 min considering the 0.54 Ma bathymetry and shoreline position. Tsunami waves propagate from the region of slope failure and rapidly propagate to the southeast. They are comparatively slower when propagating to the northwest. Bathymetry influences tsunami-wave propagation and its resulting impact on coastal areas.

with a shorter propagating distance—leading to a smaller attenuation of wave energy—result in the largest tsunami waves along the shoreline[3,21]. Tsunami waves in the 0.54 Ma scenario arrived at the nearest shoreline within 8 min, much earlier than the present-day scenario (150 min) (Table 1). The larger wave height and shorter arrival time signify greater damage to the shoreline. On the eastern shoreline, where the continental shelf is narrower (10–30 km), the similar arrival times of paleo (48 min) and present-day (47 min) models suggest that tsunami height is less sensitive to variations in bathymetry when compared to broad continental shelves (Fig. 1).

The well-studied Storegga Slide tsunami represents an important example of how bathymetry controls tsunami height and propagation. Tsunami waves triggered by the Storegga Slide at ~8200 years ago[59] were recently recognized to be 0.5–4.5 m higher in the southeast North Sea near Denmark[15], and 20 m higher around the Shetland Islands[14], when compared to previous models not taking into account paleobathymetry as a controlling factor in tsunami height[5,15]. However, in order to restore the paleobathymetry of regions affected by tsunamis, one needs to obtain a precise digital elevation model for the present-day

shoreline and seafloor, together with borehole data of enough quality to allow estimates of relative sea-level variations and sedimentation rates. Such datasets are not available for most historic landslides, explaining why most published work does not include bathymetric and morphological analyses of paleoshelves and paleoshorelines.

Conclusions

In this study, a Quaternary (0.54 Ma) submarine landslide in the northern South China Sea, and associated tsunami, were investigated using geophysical constraints and numerical models. A similar landslide occurring at present will cause catastrophic damage on the shores of the South China Sea. However, the models in this work show such as a tsunami to have generated more severe damage at 0.54 Ma because of its 180–580 km oceanward position relative to the present-day shoreline. Such a setting would result in waves at least three-times larger than at present, and very short arrival times to the coast. This study highlights the control of a variable bathymetry on tsunami propagation and its effect on the damage recorded in shoreline areas. A relative sea-level rise and low sedimentation rates can reduce

Table 1 Modeled parameters and main results pertaining to the present-day and 0.54 Ma models.

Slope failure model	Water depth (m)	Length of landslide (km)	Width of landslide (km)	Thickness of landslide (m)	Maximum wave height (m) at the northern SCS shoreline	Shortest arrival time (minute) to the northern SCS shoreline	Maximum wave height (m) at the eastern SCS shoreline	Shortest arrival time (minute) at the eastern SCS shoreline
Present-day model	940–3090	252	41	153	5	150	5	48
Ancient (0.54 Ma) model	730–2890	252	41	153	18	8	10	47

Geomorphological characteristics of the two modeled slope failure events and the maximum heights and arrival times of tsunami waves generated by the slope failures. The shortest arrival time is defined as the shortest time spanning between the onset of the slope failure and the arrival of the tsunami waves on the shoreline.
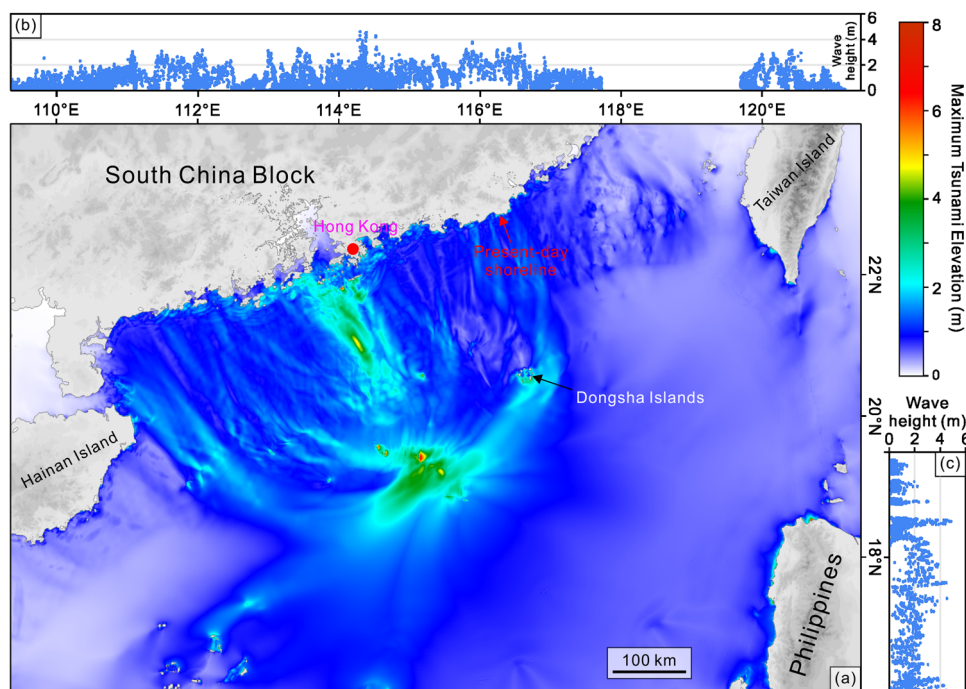*SCS* South China Sea.

Fig. 7 Maximum tsunami-wave height generated by the present-day bathymetric conditions and shoreline position. a Maximum tsunami-wave height generated by a submarine landslide considering the present-day bathymetry and shoreline position. **b** Tsunami-wave height along the shoreline of the northern South China Sea reaches a maximum of ~5 m. **c** Tsunami-wave height along the shoreline of the eastern South China Sea also reaches a maximum of ~5 m.

the impact of landslide-generated tsunamis, especially on shorelines located near broad continental shelves (e.g., northern Australia).

Methods

Geophysical data. The dataset interpreted in this study includes 23,500 km of 2D seismic profiles with a line spacing ranging from 2 to 8 km, plus 6750 km^2 of 3D seismic data comprising two volumes acquired in 2006 and 2008 (Fig. 1). The 3D seismic data were acquired using an array of tuned air-guns with a total volume of 160 in^3. A set of six 3000 m-long streamers, with a spacing of 12.5 m and 240 channels, were also used during seismic-data acquisition. At the depth of occurrence of the Baiyun Slide, the 3D seismic data have a vertical resolution of 9 m based on its main frequency of 45 Hz and a P-wave velocity of 1540 m/s[39]. The 2D seismic data were acquired from 1999 to 2002 using tuned air-guns with a 3000 m-long 120-channel streamer with a hydrophone spacing of 25 m[39]. The vertical resolution of the 2D seismic-data approaches 11 m based on their main frequency of 35 Hz.

Multibeam bathymetric data covered 25,000 km^2 of the northern South China Sea and were acquired in 2008 using a SeaBeam 2112 multibeam echo-sounder.

The SeaBeam 2112 operated at a main frequency of 12 kHz, with a pulse length of 3–20 ms. Since the depth accuracy of the acquired data is better than 0.5% of the water depth (1000–3100 m in continental-slope basins), and the full swath width of the bathymetric system approaches 120°, the vertical and horizontal resolutions of the multibeam bathymetric data are, respectively, 5.5–15.5 m and 100 m.

Paleoshoreline restoration. Shoreline progradation or retrogradation is mainly caused by geological and climatic processes such as eustatic sea-level change, tectonic uplift and subsidence, sediment deposition, and erosion. These processes can be grouped in two types: (a) relative sea-level change, which includes eustatic sea-level, tectonic uplift and subsidence, and (b) sediment thickness, pertaining to the effect of sediment accumulation and erosion. As the present-day sea level is higher than that recorded at 0.54 Ma (Supplementary Fig. S2), the models need to take this fact into account when estimating paleobathymetry—excessive accommodation space must be corrected. For the sediment thickness, we take into account the sediment accumulated in the basin to calibrate the paleobathymetry[60]. Hence, for a certain time t, the digital elevation model (DEM) of a region can be expressed as[60]:

$$\mathrm{DEM}(t) = \mathrm{DEMp} - \mathrm{RSL}(t) + \mathrm{S}(t) \qquad (1)$$

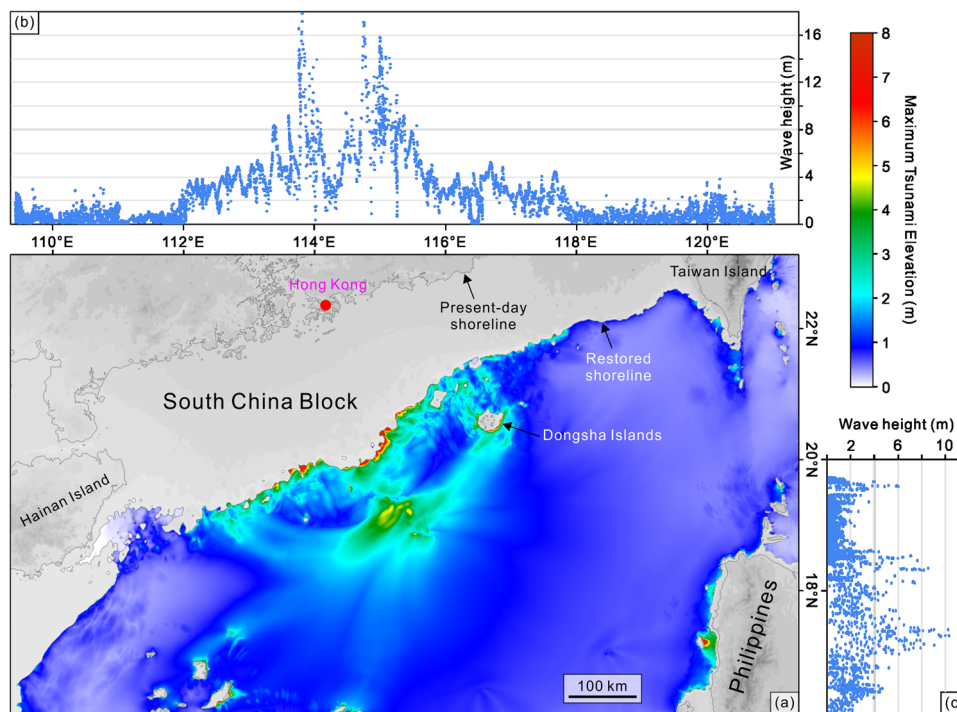where DEMp is the present-day regional bathymetry extracted from the digital

Fig. 8 Maximum tsunami-wave height generated by the 0.54 Ma bathymetric conditions and shoreline position. a Maximum tsunami-wave height generated by a submarine landslide considering the 0.54 Ma bathymetry and shoreline position. **b** Tsunami-wave height along the shoreline of the northern South China Sea reaches a maximum of ~17 m. **c** Tsunami-wave height along the shoreline of the eastern South China Sea reaches a maximum of ~10 m.

elevation model. RSL(t) is the relative sea level at time t, which S(t) is the sediment thickness from t to the present day. The parameter t is the time elapsed from the present, and it is equal to 0.54 Ma.

In this study, the present-day regional bathymetry (DEMp) was gathered from the British Oceanographic Data Centre (BODC; https://www.gebco.net/data_and_products/gridded_bathymetry_data/). Relative sea-level changes used to restore the paleoshoreline are based on data from ref. [55] for the Pearl River Mouth Basin, and information from refs. [53,54] for the Yinggehai and Qiongdongnan basins (Supplementary Fig. S2). The relative sea-level curve by ref. [55] is based on micropaleontological data collected from 43 exploration wells and variations in coastal onlap interpreted in seismic data (Fig. 1). The curves in refs. [53,54] are based on foraminifera and carbon/oxygen isotopes gathered from 10 exploration wells, as well as seismic-stratigraphic data. Sediment thickness S(t) is calculated based on the average sedimentation rates recorded at present, and used to extrapolate the total thickness of sediment accumulated since 0.54 Ma. Average sedimentation rates are estimated from exploration/ODP/IODP wells[37,61–63], gravity cores[64–66], seismic profiles[67], and published sediment thickness maps[38,58,68] (Supplementary Table S1). The acquired data span the entire northern South China Sea (Fig. 1), focusing on the areas where paleoshorelines were identified so as to meet the accuracy levels required for shoreline reconstructions.

Tsunami modeling. The two-layer non-hydrostatic model NHWAVE[24,69–71] was used to simulate the submarine landslide motion and resulting tsunami propagation. The model has been validated against a series of tsunami benchmarks[72] and was successfully applied to a number of tsunamis generated by submarine landslides[27,32,73,74]. NHWAVE is a lower-layer non-hydrostatic landslide model that simulates submarine landslides using the Newtonian viscous or granular rheology closure[11,69,75]. The lower-layer equations retain the effects of non-hydrostatic pressure, allowing the model to simulate motions over arbitrary and locally steep bathymetry[70,71]. The upper-layer non-hydrostatic wave model can solve the coupling between water waves and ground motions caused by a submarine landslide. Our models were constrained by the seismic interpretation (Fig. 3) and paleobathymetric restorations (Fig. 4). The restored paleobathymetric data were used to re-grid all bathymetric maps with a 400 × 400 m grid resolution prior to their use in NHWAVE. As tsunami wavelength is typically larger than 22 km, there are at least 20 grid points per wavelength in the model. Such a grid resolution was considered sufficient because a detailed assessment of shoreline flooding is beyond the scope of the study.

Based on the internal seismic character of MTDb (i.e., chaotic to transparent seismic reflections with no recognizable deformation, the modeled seafloor failure represents a typical debris flow (Fig. 5). According to the key parameters interpreted from geophysical data (slope gradient, length, width, thickness, and volume of submarine landslides), and also acquired from published work (laminar

viscosity and bottom friction coefficients[69–71,75]) (Supplementary Table S2), the slope failure event associated with MTDb (Fig. 5) and associated tsunami (Fig. 6) were modeled with the present-day and 0.54 Ma digital elevation models as base maps.

Data availability

The "present-day digital elevation model" data that support the findings of this study are available from the British Oceanographic Data Centre (BODC; https://www.gebco.net/data_and_products/gridded_bathymetry_data/). Sedimentation rates are shown in Supplementary Table S1 and references therein. The geophysical data are the property of the China National Offshore Oil Company, the Guangzhou Marine Geological Survey and the Second Institute of Oceanography. Restrictions apply to the availability of these data, which were used under license for the current study, and thus are not publicly available. We can, however, provide a version of the seismic profile image presented in Fig. 3—without interpretations—on request (please contact the corresponding author). The original geophysical data may be requested from the data owner.

Code availability

The modeling code that support the findings of this study is available from co-author Fengyan Shi, or via the links "https://github.com/JimKirby/NHWAVE" and "https://github.com/fengyanshi/FUNWAVE-TVD".

References

1. Berndt, C., Brune, S., Nisbet, E., Zschau, J. & Sobolev, S. V. Tsunami modeling of a submarine landslide in the Fram Strait. *Geochem. Geophys. Geosyst.* **10**, 9 (2009).
2. Goff, J. & Terry, J. P. Tsunamigenic slope failures: the Pacific Islands 'blind spot'? *Landslides* **13**, 1535–1543 (2016).
3. Grilli, S. T., Taylor, O. D. S., Baxter, C. D. P. & Maretzki, S. A probabilistic approach for determining submarine landslide tsunami hazard along the upper east coast of the United States. *Mar. Geol.* **264**, 74–97 (2009).

4. Heidarzadeh, M., Ishibe, T., Sandanbata, O., Muhari, A. & Wijanarto, A. B. Numerical modeling of the subaerial landslide source of the 22 December 2018 Anak Krakatoa volcanic tsunami, Indonesia. *Ocean Eng.* **195**, 11 (2020).

5. Hill, J., Collins, G. S., Avdis, A., Kramer, S. C. & Piggott, M. D. How does multiscale modelling and inclusion of realistic palaeobathymetry affect numerical simulation of the Storegga Slide tsunami. *Ocean Model* **83**, 11–25 (2014).

6. Hornbach, M. J. et al. High tsunami frequency as a result of combined strike-slip faulting and coastal landslides. *Nat. Geosci.* **3**, 783–788 (2010).

7. Lovholt, F., Pedersen, G., Harbitz, C. B., Glimsdal, S. & Kim, J. On the characteristics of landslide tsunamis. *Philos. Trans. R. Soc. A Math. Phys. Eng. Sci.* **373**, 18 (2015).

8. Terry, J. P., Winspear, N., Goff, J. & Tan, P. H. H. Past and potential tsunami sources in the South China Sea: a brief synthesis. *Earth Sci. Rev.* **167**, 47–61 (2017).

9. Synolakis, C. E. et al. The slump origin of the 1998 Papua New Guinea Tsunami. *Proc. R. Soc. A Math. Phys. Eng. Sci.* **458**, 763–789 (2002).

10. Tappin, D. R., Watts, P., McMurtry, G. M., Lafoy, Y. & Matsumoto, T. The Sissano, Papua New Guinea Tsunami of July 1998—offshore evidence on the source mechanism. *Mar. Geol.* **175**, 1–23 (2001).

11. Yavari-Ramshe, S. & Ataie-Ashtiani, B. Numerical modeling of subaerial and submarine landslide-generated tsunami waves-recent advances and future challenges. *Landslides* **13**, 1325–1368 (2016).

12. Madeira, J., Ramalho, R. S., Hoffmann, D. L., Mata, J. & Moreira, M. A geological record of multiple Pleistocene tsunami inundations in an oceanic island: the case of Maio, Cape Verde. *Sedimentology* **67**, 1529–1552 (2020).

13. Ramalho, R. S. et al. Hazard potential of volcanic flank collapses raised by new megatsunami evidence. *Sci. Adv.* **1**, 10 (2015).

14. Dawson, A. G. et al. Reconciling Storegga tsunami sedimentation patterns with modelled wave heights: A discussion from the Shetland Isles field laboratory. *Sedimentology* **67**, 1344–1353 (2020).

15. Fruergaard, M. et al. Tsunami propagation over a wide, shallow continental shelf caused by the Storegga slide, southeastern North Sea, Denmark. *Geology* **43**, 1047–1050 (2015).

16. Moscardelli, L., Wood, L. & Mann, P. Mass-transport complexes and associated processes in the offshore area of Trinidad and Venezuela. *AAPG Bull* **90**, 1059–1088 (2006).

17. Ten Brink, U. S., Lee, H. J., Geist, E. L. & Twichell, D. Assessment of tsunami hazard to the US East Coast using relationships between submarine landslides and earthquakes. *Mar. Geol.* **264**, 65–73 (2009).

18. Watson, S. J., Mountjoy, J. J. & Crutchley, G. J. Tectonic and geomorphic controls on the distribution of submarine landslides across active and passive margins, eastern New Zealand. *Geol. Soc. Lond. Special Publ.* **500**, 477–494 (2020).

19. Ishizawa, T., Goto, K., Yokoyama, Y. & Goff, J. Dating tsunami deposits: present knowledge and challenges. *Earth Sci. Rev.* **200**, 11 (2020).

20. Grilli, S. T. & Watts, P. Modeling of waves generated by a moving submerged body. Applications to underwater landslides. *Eng. Anal. Bound. Elem.* **23**, 645–656 (1999).

21. Heidarzadeh, M., Tappin, D. R. & Ishibe, T. Modeling the large runup along a narrow segment of the Kaikoura coast, New Zealand following the November 2016 tsunami from a potential landslide. *Ocean Eng.* **175**, 113–121 (2019).

22. Horrillo, J., Wood, A., Kim, G. B. & Parambath, A. A simplified 3-D Navier-Stokes numerical model for landslide-tsunami: application to the Gulf of Mexico. *J. Geophys. Res. Oceans* **118**, 6934–6950 (2013).

23. Kelfoun, K., Giachetti, T. & Labazuy, P. Landslide-generated tsunamis at Reunion Island. *J. Geophys. Res. Earth Surf.* **115**, 17 (2010).

24. Ma, G. F., Shi, F. Y. & Kirby, J. T. Shock-capturing non-hydrostatic model for fully dispersive surface wave processes. *Ocean Model* **43-44**, 22–35 (2012).

25. Shi, F. Y. et al. High-resolution non-hydrostatic modeling of frontal features in the mouth of the Columbia River. *Estuaries Coasts* **40**, 296–309 (2017).

26. Yalciner, A. C. et al. A possible submarine landslide and associated tsunami at the Northwest Nile Delta, Mediterranean Sea. *Oceanography* **27**, 68–75 (2014).

27. Schambach, L., Grilli, S. T., Tappin, D. R., Gangemi, M. D. & Barbaro, G. New simulations and understanding of the 1908 Messina tsunami for a dual seismic and deep submarine mass failure source. *Mar. Geol.* **421**, 20 (2019).

28. Gelfenbaum, G. & Jaffe, B. Erosion and sedimentation from the 17 July, 1998 Papua New Guinea tsunami. *Pure Appl. Geophys.* **160**, 1969–1999 (2003).

29. Grilli, S. T. et al. Modelling of the tsunami from the December 22, 2018 lateral collapse of Anak Krakatau volcano in the Sunda Straits, Indonesia. *Sci Rep* **9**, 13 (2019).

30. Carvajal, M., Araya-Cornejo, C., Sepulveda, I., Melnick, D. & Haase, J. S. Nearly instantaneous tsunamis following the Mw 7.5 2018 Palu earthquake. *Geophys. Res. Lett.* **46**, 5117–5126 (2019).

31. Omira, R. et al. The September 28th, 2018, tsunami in Palu-Sulawesi, Indonesia: a post-event field survey. *Pure Appl. Geophys.* **176**, 1379–1395 (2019).

32. Schambach, L., Grilli, S. T. & Tappin, D. R. New high-resolution modeling of the 2018 Palu Tsunami, based on supershear earthquake mechanisms and mapped coastal landslides, supports a dual source. *Front. Earth Sci.* **8**, 22 (2021).

33. Li, L. L., Shi, F. Y., Ma, G. F. & Qiu, Q. Tsunamigenic potential of the Baiyun slide complex in the south China Sea. *J. Geophys. Res. Solid Earth* **124**, 7680–7698 (2019).

34. Lovholt, F., Harbitz, C. B. & Haugen, K. B. A parametric study of tsunamis generated by submarine slides in the Ormen Lange/Storegga area off western Norway. *Mar. Petrol. Geol.* **22**, 219–231 (2005).

35. Higaki, H., Goto, K., Yanagisawa, H., Sugawara, D. & Ishizawa, T. Three thousand year paleo-tsunami history of the southern part of the Japan Trench. *Prog. Earth Planet. Sci.* **8**, 19 (2021).

36. Mutaqin, B. W. et al. Evidence of unknown paleo-tsunami events along the Alas Strait, West Sumbawa, Indonesia. *Geosciences* **11**, 20 (2021).

37. Wang, P., Prell, W. L. & Blum, P. *Proc. ODP, Init. Rept. 184 [CD-ROM]*. in Ocean Drilling Program. (eds Wang, P., Prell, W. L. & Blum, P.) 77845–79547 (Texas A & M University, 2000).

38. Xie, H. et al. Cenozoic sedimentary evolution of deepwater sags in the Pearl River Mouth Basin, northern South China Sea. *Mar. Geophys. Res.* **34**, 159–173 (2013).

39. Sun, Q. L. et al. Reconstruction of repeated quaternary slope failures in the northern South China Sea. *Mar. Geol.* **401**, 17–35 (2018).

40. Zhu, W. L. et al. Geochemistry, origin, and deep-water exploration potential of natural gases in the Pearl River Mouth and Qiongdongnan basins, South China Sea. *AAPG Bull* **93**, 741–761 (2009).

41. Megawati, K. et al. Tsunami hazard from the subduction megathrust of the South China Sea: Part I. Source characterization and the resulting tsunami. *J. Asian Earth Sci.* **36**, 13–20 (2009).

42. NGDC (National Geophysical Data Center). National Geophysical Data Center/World Data Service (NGDC/WDS): Global Historical Tsunami (2017), https://doi.org/10.7289/V5PN93H7.

43. Gee, M. J. R., Uy, H. S., Warren, J., Morley, C. K. & Lambiase, J. J. The Brunei slide: a giant submarine landslide on the North West Borneo Margin revealed by 3D seismic data. *Mar. Geol.* **246**, 9–23 (2007).

44. Sun, Y. B. et al. The geometry and deformation characteristics of Baiyun submarine landslide. *Ma. Geol. Quatern. Geol.* **28**, 69–77 (2008).

45. Li, L., Clift, P. D. & Nguyen, H. T. The sedimentary, magmatic and tectonic evolution of the southwestern South China Sea revealed by seismic stratigraphic analysis. *Mar. Geophys. Res.* **34**, 341–365 (2013).

46. He, Y., Zhong, G. F., Wang, L. L. & Kuang, Z. G. Characteristics and occurrence of submarine canyon-associated landslides in the middle of the northern continental slope, South China Sea. *Mar. Petrol. Geol.* **57**, 546–560 (2014).

47. Sun, Q. L. et al. Free gas accumulations in basal shear zones of mass-transport deposits (Pearl River Mouth Basin, South China Sea): an important geohazard on continental slope basins. *Mar. Petrol. Geol.* **81**, 17–32 (2017).

48. Sun, Q. L., Alves, T. M., Lu, X. Y., Chen, C. X. & Xie, X. N. True volumes of slope failure estimated from a quaternary mass-transport deposit in the northern South China Sea. *Geophys. Res. Lett.* **45**, 2642–2651 (2018).

49. Sun, Q. L., Xie, X. N., Piper, D. J. W., Wu, J. & Wu, S. G. Three dimensional seismic anatomy of multi-stage mass transport deposits in the Pearl River Mouth Basin, northern South China Sea: their ages and kinematics. *Mar. Geol.* **393**, 93–108 (2017).

50. Wang, L., Wu, S. G., Li, Q. P., Wang, D. W. & Fu, S. Y. Architecture and development of a multi-stage Baiyun submarine slide complex in the Pearl River Canyon, northern South China Sea. *Geo-Mar. Lett.* **34**, 327–343 (2014).

51. Wang, X. X. et al. Genesis and evolution of the mass transport deposits in the middle segment of the Pearl River canyon, South China Sea: Insights from 3D seismic data. *Mar. Petrol. Geol.* **88**, 555–574 (2017).

52. Hampton, M. A., Lee, H. J. & Locat, J. Submarine landslides. *Rev. Geophys.* **34**, 33–59 (1996).

53. Hao, Y. C., Chen, P. F., Wan, X. Q. & Dong, J. S. Late tertiary sequence stratigraphy and sea level changes in Yinggehai-Qiongdongnan Basin. *Geoscience* **14**, 237–245 (2000).

54. Su, M. et al. Controlling factors on the submarine canyon system: a case study of the Central Canyon System in the Qiongdongnan Basin, northern South China Sea. *Sci. China-Earth Sci.* **57**, 2457–2468 (2014).

55. Xu, S. C., Yang, S. K. & Huang, L. F. The application of sequence stratigraphy to stratigraphic correlation. *Earth Sci. Front.* **2**, 115–123 (1995).

56. Clift, P. D. & Sun, Z. The sedimentary and tectonic evolution of the Yinggehai-Song Hong basin and the southern Hainan margin, South China Sea: implications for Tibetan uplift and monsoon intensification. *J. Geophys. Res. Solid Earth* **111**, 28 (2006).

57. van Hoang, L., Wu, F. Y., Clift, P. D., Wysocka, A. & Swierczewska, A. Evaluating the evolution of the Red River system based on in situ U-Pb dating and Hf isotope analysis of zircons. *Geochem. Geophys. Geosyst.* **10**, 20 (2009).

58. Lei, C. *Structure and Evolution of Yinggehai and Qiongdongnan Basins, South China Sea: Implications for Cenozoic Tectonics in Southeast Asia*. PhD thesis, China University of Geosciences (Wuhan) (2012).

59. Bryn, P., Berg, K., Forsberg, C. F., Solheim, A. & Kvalstad, T. J. Explaining the storegga slide. *Mar. Petrol. Geol.* **22**, 11–19 (2005).

60. Meyer, M. & Harff, J. Modelling palaeo coastline changes of the Baltic Sea. *J. Coast. Res.* **21**, 598–609 (2005).

61. Chen, F. et al. Calcareous nannofossils and foraminifera biostratigraphy on the northeastern slope of the South China Sea and variation in sedimentation rates. *Earth Sci.* **41**, 416–424 (2016).

62. Li, Q. Y. et al. A 33 Ma lithostratigraphic record of tectonic and paleoceanographic evolution of the South China Sea. *Mar. Geol.* **230**, 217–235 (2006).

63. Wang, G., Chu, F. & Wang, C. Paleoelevation reconstruction of Red River drainage areas in Western Yunnan Plateau since Miocene. *J. Chengdu University Technol.* **31**, 118–124 (2004).

64. Xu, Z. F. Sedimentary rates and changing mechanism in northern and middle South China Sea since Late Pleistocene. *J. Oceanogr. Taiwan Strait* **14**, 356–360 (1995).

65. Xue, L. Y., Ding, X., Pei, R. J. & Wan, X. Q. Miocene evolution of palaeo-water depth and subsidence revealed in Well LF14 from Lufeng Sag, northern South China Sea. *J. Tropical Oceanogr.* **37**, 72–83 (2018).

66. Yue, Y. Z. 14C dating of the deep-sea sediments from the central South China Sea. *Donghai Mar. Sci.* **5**, 153–157 (1987).

67. Zhao, Z. X. et al. The high resolution sedimentary filling in Qiongdongnan Basin, Northern South China Sea. *Mar. Geol.* **361**, 11–24 (2015).

68. Xu, Z., Wang, M., Hong, A., Guo, F. & Liu, G. Ages of sediments and sedimentation rates of the western Taiwan Strait since late Pleistocene. *J. Oceanogr. Taiwan Strait* **8**, 114–122 (1989).

69. Ma, G. F., Kirby, J. T., Hsu, T. J. & Shi, F. Y. A two-layer granular landslide model for tsunami wave generation: theory and computation. *Ocean Model.* **93**, 40–55 (2015).

70. Zhang, C., Kirby, J. T., Shi, F. Y., Ma, G. F. & Grilli, S. T. A two-layer non-hydrostatic landslide model for tsunami generation on irregular bathymetry. 2. Numerical discretization and model validation. *Ocean Model.* **160**, 22 (2021).

71. Zhang, C., Kirby, J. T., Shi, F. Y., Ma, G. F. & Grilli, S. T. A two-layer non-hydrostatic landslide model for tsunami generation on irregular bathymetry. 1. Theoretical basis. *Ocean Model.* **159**, 14 (2021).

72. Kirby, J. T. et al. Validation and inter-comparison of models for landslide tsunami generation. *Ocean Model.* **170**, 28 (2022).

73. Grilli, S. T. et al. Modeling coastal tsunami hazard from submarine mass failures: effect of slide rheology, experimental validation, and case studies off the US East Coast. *Nat. Hazards* **86**, 353–391 (2017).

74. Tappin, D. R. et al. Did a submarine landslide contribute to the 2011 Tohoku tsunami. *Mar. Geol.* **357**, 344–361 (2014).

75. Kirby, J. T., Shi, F. Y., Nicolsky, D. & Misra, S. The 27 April 1975 Kitimat, British Columbia, submarine landslide tsunami: a comparison of modeling approaches. *Landslides* **13**, 1421–1434 (2016).

76. Milliman, J. D. & Farnsworth, K. L. *River Discharge to the Coastal Ocean: A Global Synthesis* (Cambridge University Press, 2011).

Author contributions

Q.L.S. and Q.W. equally contributed to the conception/design of the work, analysis/interpretation of data and numerical models, and drafted the manuscript; F.Y.S. contributed to the design of the work and creation of new software, and participated in drafting the manuscript; T.A., S.G., and X.N.X. contributed to the analysis/interpretation of data, and participated in the writing and revision of the manuscript; S.G.W. and J.B.L. contributed to acquisition/analysis/interpretation of data, and participated in the revision of the manuscript.

Competing interests

The authors declare no competing interests.

Additional information

Supplementary information The online version contains supplementary material available at https://doi.org/10.1038/s43247-022-00572-w.

Correspondence and requests for materials should be addressed to Qiliang Sun or Shiguo Wu.

Peer review information *Communications Earth & Environment* thanks Maureen Walton, David Tappin and the other, anonymous, reviewer(s) for their contribution to the peer review of this work. Primary Handling Editors: João Duarte, Joe Aslin.

Reprints and permission information is available at http://www.nature.com/reprints

Publisher's note Springer Nature remains neutral with regard to jurisdictional claims in published maps and institutional affiliations.